

## Article

# Remarkable Reduction in $I_G$ with an Explicit Investigation of the Leakage Conduction Mechanisms in a Dual Surface-Modified $\text{Al}_2\text{O}_3/\text{SiO}_2$ Stack Layer AlGaN/GaN MOS-HEMT

Soumen Mazumder <sup>1</sup>, Parthasarathi Pal <sup>1</sup>, Kuan-Wei Lee <sup>2</sup> and Yeong-Her Wang <sup>1,\*</sup><sup>1</sup> Department of Electrical Engineering, Institute of Microelectronics, National Cheng-Kung University, Tainan 701, Taiwan<sup>2</sup> Department of Electronic Engineering, I-Shou University, Kaohsiung 840, Taiwan

\* Correspondence: yhw@ee.ncku.edu.tw; Tel.: +886-6-275-7575-62352; Fax: +886-6-2080598

**Abstract:** We demonstrated the performance of an  $\text{Al}_2\text{O}_3/\text{SiO}_2$  stack layer AlGaN/GaN metal-oxide semiconductor (MOS) high-electron-mobility transistor (HEMT) combined with a dual surface treatment that used tetramethylammonium hydroxide (TMAH) and hydrochloric acid (HCl) with post-gate annealing (PGA) modulation at 400 °C for 10 min. A remarkable reduction in the reverse gate leakage current ( $I_G$ ) up to  $1.5 \times 10^{-12}$  A/mm (@  $V_G = -12$  V) was observed in the stack layer MOS-HEMT due to the combined treatment. The performance of the dual surface-treated MOS-HEMT was significantly improved, particularly in terms of hysteresis, gate leakage, and subthreshold characteristics, with optimized gate annealing treatment. In addition, an organized gate leakage conduction mechanism in the AlGaN/GaN MOS-HEMT with the  $\text{Al}_2\text{O}_3/\text{SiO}_2$  stack gate dielectric layer was investigated before and after gate annealing treatment and compared with the conventional Schottky gate. The conduction mechanism in the reverse gate bias was Poole–Frankel emission for the Schottky-gate HEMT and the MOS-HEMT before annealing. The dominant conduction mechanism was ohmic/Poole–Frankel at low/medium forward bias. Meanwhile, gate leakage was governed by the hopping conduction mechanism in the MOS-HEMT without gate annealing modulation at a higher forward bias. After post-gate annealing (PGA) treatment, however, the leakage conduction mechanism was dominated by trap-assisted tunneling at the low to medium forward bias region and by Fowler–Nordheim tunneling at the higher forward bias region. Moreover, a decent product of maximum oscillation frequency and gate length ( $f_{\text{max}} \times L_G$ ) was found to reach 27.16 GHz· $\mu\text{m}$  for the stack layer MOS-HEMT with PGA modulation. The dual surface-treated  $\text{Al}_2\text{O}_3/\text{SiO}_2$  stack layer MOS-HEMT with PGA modulation exhibited decent performance with an  $I_{\text{DMAX}}$  of 720 mA/mm, a peak extrinsic transconductance ( $G_{\text{MMAX}}$ ) of 120 mS/mm, a threshold voltage ( $V_{\text{TH}}$ ) of  $-4.8$  V, a higher  $I_{\text{ON}}/I_{\text{OFF}}$  ratio of approximately  $1.2 \times 10^9$ , a subthreshold swing of 82 mV/dec, and a cutoff frequency ( $f_t$ )/maximum frequency of ( $f_{\text{max}}$ ) of 7.5/13.58 GHz.

**Keywords:**  $\text{Al}_2\text{O}_3/\text{SiO}_2$ ; AlGaN/GaN; MOS-HEMT; post-gate annealing (PGA)

**Citation:** Mazumder, S.; Pal, P.; Lee, K.-W.; Wang, Y.-H. Remarkable Reduction in  $I_G$  with an Explicit Investigation of the Leakage Conduction Mechanisms in a Dual Surface-Modified  $\text{Al}_2\text{O}_3/\text{SiO}_2$  Stack Layer AlGaN/GaN MOS-HEMT. *Materials* **2022**, *15*, 9067.

<https://doi.org/10.3390/ma15249067>

Academic Editors: Marina N. Rumyantseva and Marco Girolami

Received: 25 October 2022

Accepted: 14 December 2022

Published: 19 December 2022

**Publisher's Note:** MDPI stays neutral with regard to jurisdictional claims in published maps and institutional affiliations.



**Copyright:** © 2022 by the authors. Licensee MDPI, Basel, Switzerland. This article is an open access article distributed under the terms and conditions of the Creative Commons Attribution (CC BY) license (<https://creativecommons.org/licenses/by/4.0/>).

## 1. Introduction

Considering the unique features of III-nitride, e.g., high carrier density ( $\sim 10^{13}/\text{cm}^3$ ), large band gap ( $\sim 3.4$  eV), high saturation velocity ( $\sim 2 \times 10^7$  cm/s), and large breakdown field ( $>3$  MV/cm), extensive research has been conducted on AlGaN/GaN high-electron-mobility transistors (HEMTs) for high-power and high-frequency applications [1–3]. The high-density and high-mobility two-dimensional electron gas (2DEG) generated at the AlGaN/GaN interface enables us to understand how a power-switching transistor with low ON resistance is relevant to next-generation power conversion systems [4]. However, the performance of this type of transistor is inherently limited by high gate leakage current

( $I_G$ ) due to the strong polarization-induced electric field and Schottky gate contact [5]. The high gate leakage leads to a limited gate voltage swing (GVS), reduced radio frequency (RF) performance, and breakdown voltage ( $V_{BR}$ ).

Moreover,  $Cl_2$ -based inductive coupled plasma (ICP) dry etching has been extensively used to isolate devices. This process correspondingly induces trap states in a device, leading to severe gate leakage current [6]. Lee et al. reported that surface conditions, e.g., the native oxide layer on the GaN surface or ICP etching damage, also severely affect device performance [7]. Thus, the native oxide layer or ICP etching damage must be removed from the surface to improve device performance. Numerous wet chemical solutions, including sulfuric acid ( $H_2SO_4$ ), hydrogen fluoride (HF), hydrochloric acid (HCl), potassium hydroxide (KOH), and tetramethylammonium hydroxide (TMAH), have been used to improve the surface condition of devices [8–15]. Previous reports have suggested that TMAH surface treatment prior to gate oxide deposition can effectively enhance the performance of GaN HEMT devices to a considerable extent [7].

In addition to wet surface treatment, inserting a dielectric layer or stack structure under the metal gate can effectively suppress  $I_G$ , improve current collapse, and provide better linearity [16]. Various dielectric materials, e.g., AlN [17],  $SiO_2$  [18], MgCaO [19],  $HfO_2$  [20],  $Al_2O_3$  [21],  $HfAlO_x$  [22],  $ZrO_2$  [23], and  $TiO_2$  [24], have been extensively investigated. Among these materials,  $Al_2O_3$  is a potential candidate for fabricating a metal-oxide semiconductor (MOS)–HEMT due to its comparatively high dielectric constant ( $\sim 9$  eV), large bandgap ( $\sim 6.5$  eV) with a significant conduction band offset ( $\sim 1.91$  eV), and good interface with AlGaIn [25,26]. However, to reduce the gate leakage current further and improve the conduction band offset, a thin layer of  $SiO_2$  with a larger bandgap ( $\sim 9$  eV) can be inserted under the  $Al_2O_3$  layer [18]. Nevertheless, the interface traps between the stack gate dielectric ( $Al_2O_3/SiO_2$ ) and the (Al)GaIn layer affect the performance of the MOS–HEMT. A previous report suggested that post-gate annealing (PGA) is an effective method for reducing the oxide defect charge, interface-trapped charge, and oxide-trapped charge [27].

To reduce  $I_G$  further, and thus, improve device reliability and increase GVS, the gate leakage mechanism in AlGaIn/GaN-based MOS–HEMTs before and after gate annealing should be investigated. Previous reports have indicated that Poole–Frankel emission (PFE), trap-assisted tunneling (TAT), and Fowler–Nordheim tunneling (FNT) are the dominant leakage mechanisms in the atomic layer deposition (ALD) of  $Al_2O_3$ /AlGaIn/GaN and the low-power chemical vapor deposition (CVD) of the  $SiN_x$ /AlGaIn/GaN MOS–HEMT [28,29]. However, they have only investigated forward bias gate leakage characteristics. Although the forward and reverse leakage mechanisms of a  $SiN_x$  MOS–HEMT were investigated previously in detail, the changes in the conduction mechanism after annealing were not considered [5]. To date, no report is available on the explicit investigation of the gate leakage conduction mechanism in a dual surface-treated  $Al_2O_3/SiO_2$  stack layer MOS–HEMT before and after gate annealing modulation.

With this objective, this work demonstrated the improved device performance with a remarkable reduction in the gate leakage current of a dual surface-treated  $Al_2O_3/SiO_2$  stack layer MOS–HEMT with PGA modulation. A detailed investigation of the conduction mechanism of gate leakage current in forward and reverse biases was performed on a MOS–HEMT before and after gate annealing treatment, and the results demonstrated how the dominant conduction mechanism was changed after PGA treatment. The dual surface-treated  $Al_2O_3/SiO_2$  stack layer MOS–HEMT with PGA modulation exhibited decent performance with a maximum drain current ( $I_{D_{MAX}}$ ) of 720 mA/mm, a peak extrinsic transconductance ( $G_{M_{MAX}}$ ) of 120 mS/mm, a threshold voltage ( $V_{TH}$ ) of  $-4.8$  V, a higher  $I_{ON}/I_{OFF}$  ratio of approximately  $1.2 \times 10^9$ , a subthreshold swing (SS) of 82 mV/dec, and a cutoff frequency ( $f_t$ )/maximum frequency ( $f_{max}$ ) of 7.5/13.58 GHz, with the lowest gate leakage current of  $1.5 \times 10^{-12}$  A/mm and a decent ( $f_{max} \times L_G$ ) of 27.16 GHz· $\mu$ m.

## 2. Materials and Methods

The AlGaN/GaN epitaxy was grown using a low-pressure metal-organic chemical vapour deposition (MOCVD) system on a p-type low-resistive (111) Si substrate. The epilayers consisted 3.9  $\mu\text{m}$  GaN buffer layer, a 300 nm undoped GaN layer, a 20 nm  $\text{Al}_{0.25}\text{Ga}_{0.75}\text{N}$  barrier layer, and a 2 nm GaN cap layer. The measured sheet carrier concentration and Hall mobility were  $6.15 \times 10^{12}/\text{cm}^2$  and  $2338 \text{ cm}^2/\text{V}\cdot\text{s}$ , respectively.

Device processing started with mesa isolation by using an ICP reactive ion etching system with a  $\text{Cl}_2/\text{BCl}_3$  gas mixture. Then, the sample was immersed into 5% TMAH solution at  $85^\circ\text{C}$  for 1 min to remove native oxide and ICP etching damage. Thereafter, the source and the drain regions were defined via ultraviolet (UV) photolithography. Then, Ti/Al/Ni/Au (25/150/30/120 nm) metal contacts were deposited using an electron beam (e-beam) evaporator system, followed by rapid thermal annealing at  $875^\circ\text{C}$  for 30 s under  $\text{N}_2$  ambient atmosphere to ensure good ohmic contact. Subsequently, HCl wet treatment was performed for 3 min prior to gate metal deposition for conventional HEMT and gate oxide deposition for MOS-HEMT. Then, a stack gate dielectric layer composed of a 5 nm  $\text{SiO}_2$  followed by a 10 nm  $\text{Al}_2\text{O}_3$  layer, was deposited using an ALD system (Picosun) at  $250^\circ\text{C}$ . Finally, the gate region was defined via UV photolithography, and a Ni/Au (80/100 nm) gate stack was deposited using an e-beam evaporator followed by a liftoff process. To improve device performance further, PGA was performed at  $400^\circ\text{C}$  for 10 min. Sheet resistance was  $434 \Omega/\square$ . For reference, a MOS-HEMT with 5 nm  $\text{SiO}_2$  gate dielectric and a conventional HEMT were also fabricated. The gate width ( $W_G$ ) and gate length ( $L_G$ ) were  $100 \mu\text{m}$  and  $2 \mu\text{m}$  for all devices, and  $L_{GD}$  and  $L_{SG}$  were both  $2 \mu\text{m}$ . To understand the gate annealing treatment on the MOS-HEMT and the conventional HEMT, all devices were fabricated following the same processing conditions without PGA treatment. Figure 1a,b shows the typical schematic of a MOS-HEMT and a planar HEMT. UV photolithography was performed using an MJB3 Karl Suss mask aligner system. DC I-V and RF performance were measured with a B1500A semiconductor characterization system and an Agilent N5245A network analyzer with an HP 4142B DC monitor, respectively. To understand the gate dielectric thickness we used transmission electron microscopy (TEM) (JEOL JEM-2100F) system. After the focused ion beam, we used carbon lacey grid for better resolution of the TEM image. To understand the quantitative analysis of the surface composition and material elemental composition we did X-ray photoelectron spectroscopy (XPS) (JEOL). To analyze the effect of TMAH wet surface treatment on the performance of the stack layer MOS-HEMT device, XPS was conducted using a k-alpha X-ray photoelectron spectrometer. To stick the sample on the holder for XPS a copper foil conductive has been used. A monochromatic Al  $K\alpha$  X-ray source with  $90^\circ$  taken off-angle was used. The sputtering depth was approximately 30–50 nm.

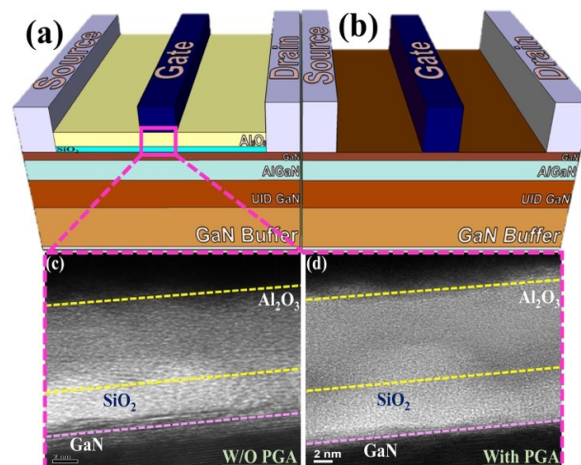


**Figure 1.** Schematic of (a)  $\text{Al}_2\text{O}_3/\text{SiO}_2$  MOS-HEMT and (b) conventional HEMT. TEM images of the MOS-HEMT (c) without gate annealing and (d) with gate annealing treatment.

### 3. Results

Figure 1c,d shows the TEM image of the  $\text{Al}_2\text{O}_3/\text{SiO}_2$  MOS–HEMT before and after gate annealing treatment. Clear layers of the 5 nm  $\text{SiO}_2$  and 10 nm  $\text{Al}_2\text{O}_3$  were found without intermixing before PGA treatment. Owing to the diffusion of atoms, a less layered structure was observed after gate annealing treatment. Typical atomic force microscopy (AFM) images are shown in Figure 2a–e under different conditions. As shown in Figure 2a,b, side wall surface morphology was improved with TMAH surface treatment. After dual surface treatment with PGA modification, the root-mean-square roughness was significantly improved from 0.70 nm to 0.24 nm, subsequently enhancing device performance.

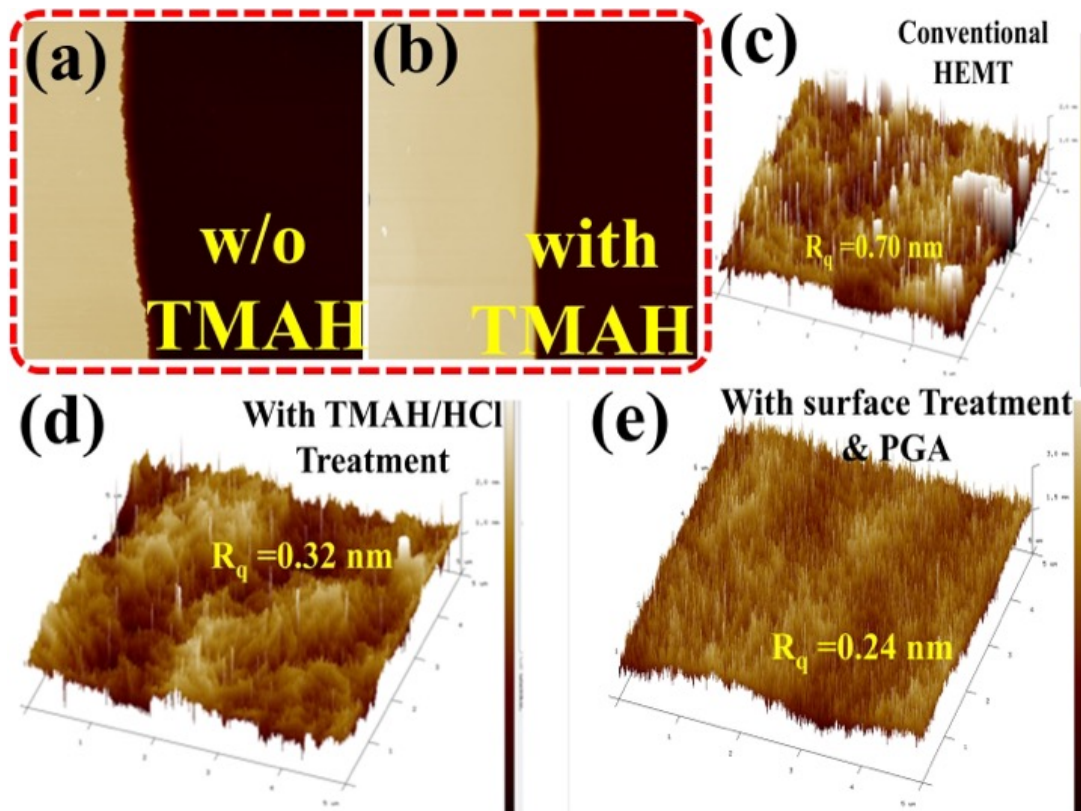


**Figure 2.** AFM profile of AlGaN/GaN device after ICP mesa etching (a) without and (b) with TMAH treatment. The 3D AFM images of the device (c) without, (d) with dual surface treatment and gate annealing modulation.

Figure 3 illustrates the change in the atomic composition of the Ga 3 core levels before and after surface treatment, with both spectra deconvoluted into two peaks of Ga–N and Ga–O. The Ga  $3d_{5/2}$  and  $\text{Ga}_2\text{O}_3$  ( $\text{Ga}^{3+}$ ) peaks were de-convoluted by considering spin-orbital splitting [30]. Figure 3 clearly shows that the intensity of Ga–O is considerably lower after TMAH surface treatment. The peak intensity ratio of Ga–O/Ga–N significantly decreased to 6.6% from 63%. The removal of native oxide at the GaN surface via wet surface treatment reduced the intensity of the Ga–O bond, subsequently improving device performance as previously reported [31–34].

The typical drain current versus voltage ( $I_D$ – $V_D$ ) characteristics of the conventional HEMT and the  $\text{Al}_2\text{O}_3/\text{SiO}_2$  stack layer MOS–HEMT are shown in Figure 4. The  $I_{D\text{MAX}}$  of the dual surface-treated stack layer ( $\text{SiO}_2$ ) MOS–HEMT and the conventional HEMT was 720 mA/mm (650 mA/mm) (@  $V_G = 3$  V) and 520 mA/mm (@  $V_G = 1$  V), respectively, with PGA modulation, as shown in Figure 4. Better pinch-off behavior in the stack layer MOS–HEMT suggested better gate controllability than in the  $\text{SiO}_2$  MOS–HEMT. The conventional HEMT was not biased with higher  $V_G$  due to the large late leakage current. The reduction of  $I_{D\text{MAX}}$  in the conventional HEMT was attributed to the large  $I_C$  [35]. Moreover,

$I_{D\text{MAX}}$  was 650 mA/mm (500 mA/mm) for the MOS–HEMT (HEMT) without annealing modulation. In addition, the ON resistance ( $R_{\text{ON}}$ ) was significantly reduced from 6.3  $\Omega\cdot\text{mm}$  to 4.9  $\Omega\cdot\text{mm}$  in the MOS–HEMT due to dual surface treatment with the application of a stack dielectric layer.

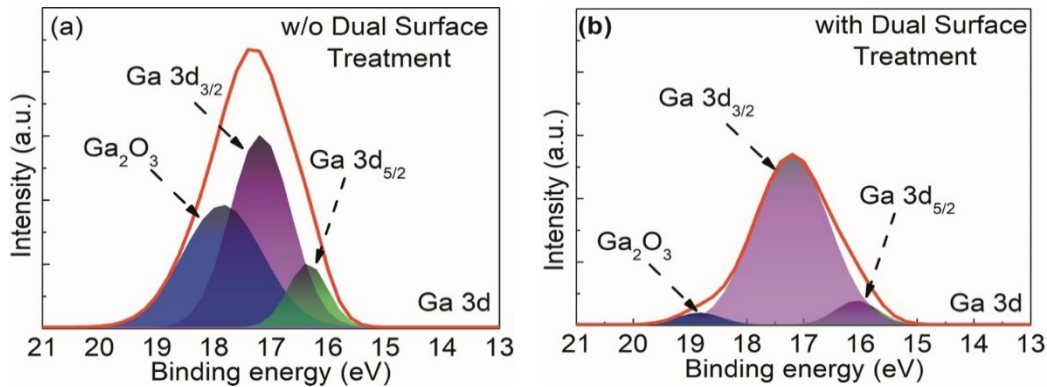


Figure 3. XPS of the AlGaIn/GaN device (a) without and (b) with dual surface treatment.

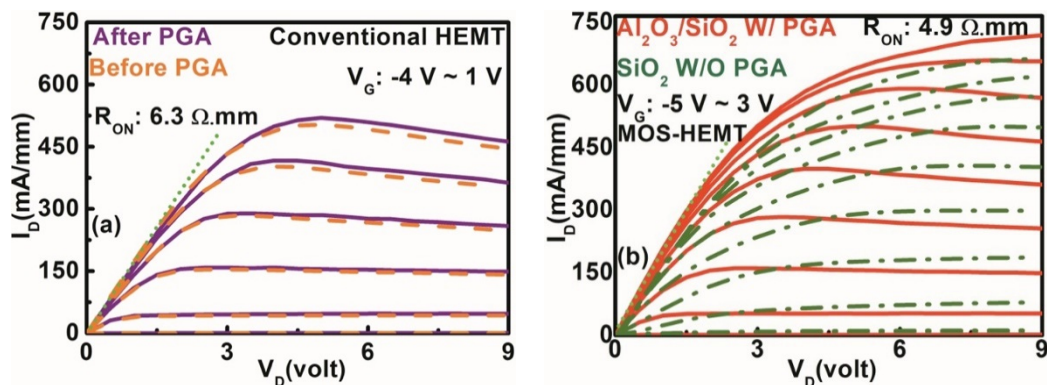
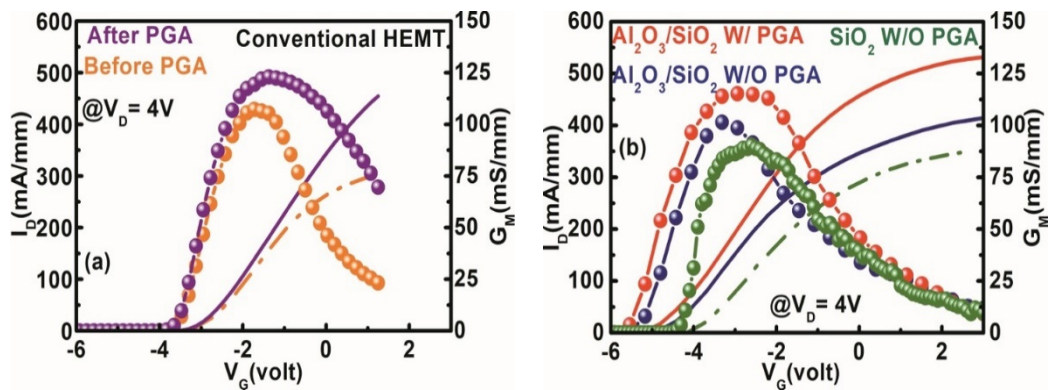


Figure 4.  $I_D$ – $V_D$  characteristics of (a) conventional HEMT with and without gate annealing and (b)  $\text{Al}_2\text{O}_3/\text{SiO}_2$  MOS–HEMT with and without gate annealing treatment and  $\text{SiO}_2$  MOS–HEMT without PGA treatment.

The transfer characteristics of the stack layer MOS–HEMT and the conventional HEMT before and after gate annealing treatment (@  $V_D = 4$  V) are shown in Figure 5. The  $\text{Al}_2\text{O}_3/\text{SiO}_2$  stack layer MOS–HEMT exhibited a  $V_{\text{TH}}$  of  $-4.8$  V ( $-4.4$  V) with (without) gate annealing modulation. For the conventional HEMT and the  $\text{SiO}_2$  MOS–HEMT,  $V_{\text{TH}}$  was  $-2.7$  V and  $-3.6$  V, respectively. The threshold voltage is defined as the gate bias intercept point of the linear extrapolation of the drain current at  $G_{\text{MMAX}}$  [22]. The  $V_{\text{TH}}$  difference between HEMT and MOS–HEMT can be expressed as [5]:

$$V_{\text{TH,MOS-HEMT}} - V_{\text{TH,HEMT}} = - \left( \frac{Q_{\text{int}}}{\epsilon_{\text{ox}}} \right) \cdot t_{\text{ox}} - \left( \frac{qn_{\text{ox}}}{2\epsilon_{\text{ox}}} \right) \cdot t_{\text{ox}}^2, \quad (1)$$

where  $Q_{\text{int}}$  is the total interface charge,  $t_{\text{ox}}$  is the thickness of the dielectric layer,  $\epsilon_{\text{ox}}$  is the effective dielectric constant of the stack dielectric layer, and  $n_{\text{ox}}$  is the oxide bulk charge. In accordance with Equation (1), the negative shift of  $V_{\text{TH}}$  is attributable to the increment of the interface fixed charge at the interface and oxide layers and the increase in the 2DEG concentration after passivation [36–38]. Moreover, the increase in separation between the gate and the channel layer may be another reason for the negative shifting of  $V_{\text{TH}}$ . The shift of  $V_{\text{TH}}$  to the reverse direction with gate annealing treatment was confirmed in Figure 5b.



**Figure 5.**  $I_D$ – $V_G$  characteristics of (a) conventional HEMT with and without gate annealing and (b)  $\text{Al}_2\text{O}_3/\text{SiO}_2$  MOS–HEMT with and without gate annealing treatment, and  $\text{SiO}_2$  MOS–HEMT without PGA treatment.

An improvement in peak extrinsic transconductance ( $G_{\text{MMAX}}$ ) was observed in the dual surface-treated  $\text{Al}_2\text{O}_3/\text{SiO}_2$  stack layer MOS–HEMT after gate annealing modulation compared with the  $\text{SiO}_2$  MOS–HEMT or the conventional HEMT shown in Figure 5. The  $G_{\text{MMAX}}$  values were 120 mS/mm (102 mS/mm) and 123 mS/mm (110 mS/mm) in the stack layer MOS–HEMT and the conventional HEMT with annealing (without annealing) modulation. The insertion of the two gate dielectrics increased the distance between the gate and the 2DEG channel, reducing gate controllability and decreasing  $G_{\text{MMAX}}$  in MOS–HEMT. In addition, GVS, defined as the 10% drop in maximum transconductance, was calculated for both devices to understand the linearity behavior of the device [20]. GVS improved from 1.10 V to 1.92 V in the dual surface-treated stack layer MOS–HEMT after gate annealing treatment. Thus, low phase noise, device linearity, and wide dynamic range were improved after dual surface treatment and PGA modulation in the stack layer MOS–HEMT [39]. Moreover,  $G_{\text{MMAX}}$  was 91 mS/mm in the  $\text{SiO}_2$  MOS–HEMT.

Figure 6 shows the subthreshold characteristics as a function of gate voltage ( $@ V_D = 4$  V) for all devices. In this figure, the subthreshold drain leakage current was decreased by more than three orders of magnitude in the  $\text{Al}_2\text{O}_3/\text{SiO}_2$  MOS–HEMT after gate annealing modulation compared with that of the conventional HEMT. The subthreshold drain leakage current was influenced by the reverse bias gate leakage current in the pinch-off region [39]. Given that  $I_G$  was suppressed by the combined effects of the stack layer gate dielectric and dual surface treatment with PGA modulation in MOS–HEMT, as discussed later, the subthreshold drain leakage current was decreased to a considerable extent. Subthreshold swing (SS) also depends on  $I_G$ . The SS values of different devices were extracted from Figure 6. The SS values were improved from 130 mV/dec to 82 mV/dec in the stack layer MOS–HEMT after gate annealing treatment. Meanwhile, for the conventional HEMT ( $\text{SiO}_2$  MOS–HEMT), the SS value was 178 mV/dec (91 mV/dec). The current ON/OFF ( $I_{\text{ON}}/I_{\text{OFF}}$ ) ratios were  $1.2 \times 10^9$  and  $5.8 \times 10^7$  for the stack layer MOS–HEMT with and without PGA treatment. By contrast, no significant improvement in the current ratio was found in the planar HEMT after gate annealing treatment.

The reverse and forward gate leakage current ( $I_G$ – $V_G$ ) characteristics of the dual surface-treated stack layer MOS–HEMT before and after gate annealing treatment and the Schottky gate HEMT without PGA were measured, and the results are presented in Figure 7. The reverse gate leakage current ( $@ V_G = -12$  V) of the  $\text{Al}_2\text{O}_3/\text{SiO}_2$  MOS–HEMT was  $2.3 \times 10^{-8}$  A/mm before gate annealing treatment. Evidently,  $I_G$  was significantly reduced by four orders of magnitude to  $1.5 \times 10^{-12}$  A/mm after annealing treatment with dual surface modification. The insertion of large bandgap materials as gate dielectric combined with dual surface treatment and PGA modulation reduced  $I_G$  to a considerable extent.

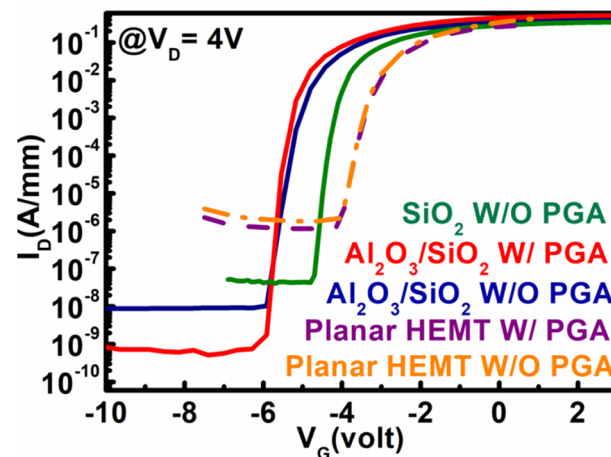


Figure 6. Subthreshold characteristics of conventional HEMT and  $\text{Al}_2\text{O}_3/\text{SiO}_2$  MOS-HEMT with and without gate annealing treatment and  $\text{SiO}_2$  MOS-HEMT without PGA treatment.

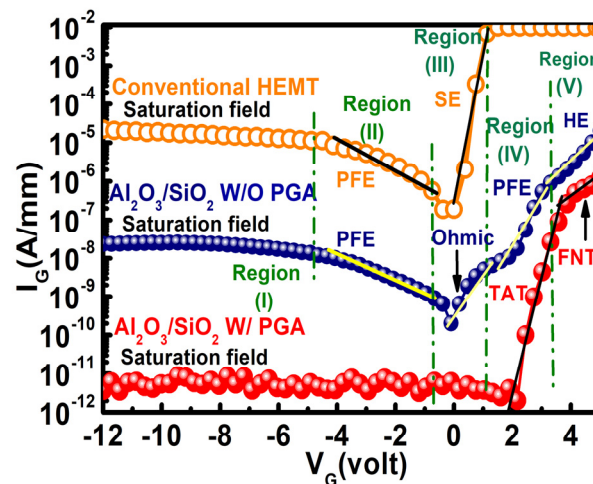


Figure 7. Gate leakage characteristics of the  $\text{Al}_2\text{O}_3/\text{SiO}_2$  MOS-HEMT with and without PGA treatment and conventional HEMT without PGA treatment.

To explore the charge of transportation mechanisms responsible for the gate leakage phenomenon,  $I_G$ - $V_G$  characteristics were divided into five regions as indicated in Figure 7. Leakage characteristics were analyzed in different regions to determine the dominant leakage mechanism for each particular region. The multiple conduction mechanism was studied to justify the appropriate charge transport phenomenon in the stack layer MOS-HEMT before and after gate annealing treatment and conventional HEMT. The conduction band edge diagram of the MOS-HEMT before and after PGA treatment and HEMT under different operating regions that illustrated the conduction mechanisms is shown in Figure 8.

### 3.1. Gate Leakage Mechanisms in the AlGaIn/GaN MOS-HEMT before Gate Annealing

For the stack layer MOS-HEMT before annealing treatment, as indicated in Region (I) for  $V_G \leq V_{TH}$ , the leakage current was saturated due to the saturation of the vertical electrical fields across the gate dielectric and the barrier layer [5]. However, the  $I_G$ - $V_G$  characteristics in Region (II) exhibited dependency on the applied electric field, and the PFE mechanism clearly dominated this region, as suggested in the fitted curve of  $[\ln(I/V) \text{ vs. } V^{1/2}]$  in Figure 9a. A comparatively high electric field supported the PFE conduction depicted

in the fitted Figure 9a, and the charge transferred through a trap shown in the band edge diagram in Figure 8a in this region exhibited the following relation [5,40]:

$$\ln\left(\frac{J_{PFE}}{E_{Di}}\right) = m\sqrt{E_{Di}} + c \quad (2)$$

$$m = \frac{q}{kT} \sqrt{\frac{q}{\pi\epsilon_{Di}}} \quad (3)$$

where  $\epsilon_{Di}$  is the permittivity of the dielectric materials,  $k_B$  is the Boltzmann's constant,  $T$  is the temperature, and  $q$  is the electronic charge. The effective dielectric constant ( $\epsilon_{Di}$ ) was extracted to 7.2 from the  $\ln(I/V)$  vs  $V^{1/2}$  characteristics, which was sufficiently close to the calculated effective dielectric constant of the  $\text{Al}_2\text{O}_3/\text{SiO}_2$  layer [41].

The dominant leakage conduction mechanism in Region (III) was ohmic due to the linear relationship of  $\ln(I)$  vs.  $\ln(V)$ , with a slope value close to 1, as shown in Figure 9b. The leakage mechanism was assumed to be PFE at a comparatively higher voltage region. The linear fitting in Figure 9c further confirmed PFE conduction because electrons can be de-trapped with an increased electric field as shown in the band edge diagram in Figure 8b. In addition, the dominant conduction mechanism in a high field region ( $V_G \geq 3$  V) was satisfied with hopping conduction from the fitted curve of  $\ln(I)$  vs.  $V$ , as shown in Figure 9d. Hopping distance ( $\lambda$ ) can be extracted from the fitted curve by considering the following equation [40,42]:

$$J = qn\lambda \exp\left(\frac{q\lambda E - E_a}{kT}\right) \quad (4)$$

where  $n$  is the electron concentration,  $f$  is the thermal vibration frequency of the trapping sites,  $E$  is the corresponding electric field, and  $E_a$  is the activation energy. The hopping distance was calibrated to 0.47 nm by using Equation (4). The electrons can overcome the hopping distance ( $\lambda$ ) in the higher field region, as shown in Figure 8c, due to the higher energy.

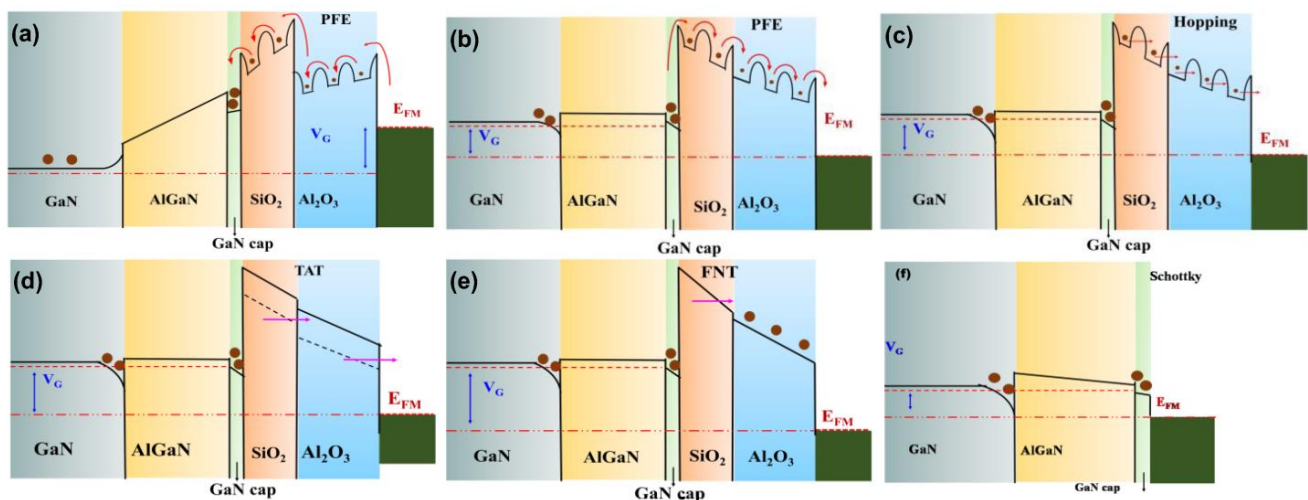


**Figure 8.** Conduction band edge diagram of  $\text{Al}_2\text{O}_3/\text{SiO}_2$  MOS-HEMT (a–c) before and (d), (e) after PGA treatment, and (f) conventional HEMT under different operating regions and showing the dominant conduction mechanism at each region.

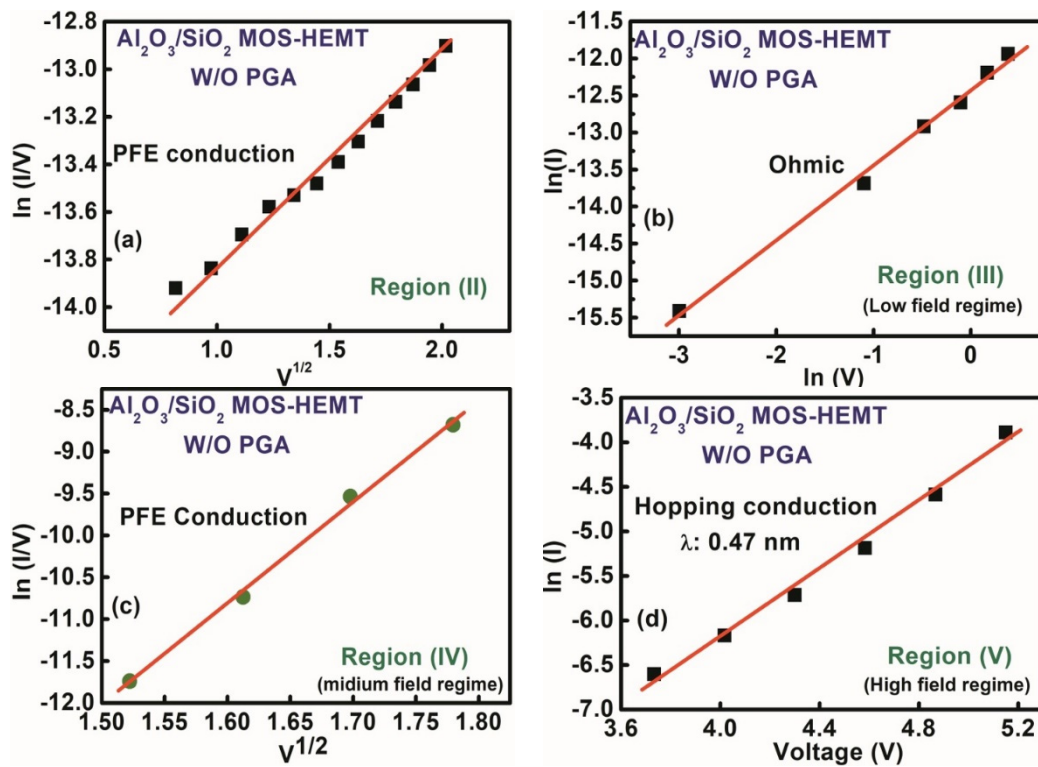


**Figure 9.** Gate leakage conduction mechanism of the Al<sub>2</sub>O<sub>3</sub>/SiO<sub>2</sub> MOS–HEMT before gate annealing treatment (a) region II, (b) region III, (c) region IV, (d) region V.

### 3.2. Gate Leakage Mechanisms in the AlGaN/GaN MOS–HEMT after Gate Annealing

The leakage mechanism of the Al<sub>2</sub>O<sub>3</sub>/SiO<sub>2</sub> MOS–HEMT after gate annealing modulation was also investigated as shown in Figure 10. After gate annealing modulation, shallow traps were reduced [39] and I<sub>G</sub> was independent of gate voltage at V<sub>G</sub> ≤ 2 V due to the saturation of the electric field [5]. The conduction band diagram in Region (IV) for the stack layer MOS–HEMT after annealing treatment is shown in Figure 8d. In this region, leakage transportation was estimated from the fitting curve of [ln(I) vs. 1/V], as shown in Figure 10a, to a two-step TAT mechanism. The electric field dependence of the TAT current (J<sub>TAT</sub>) is given by the following equation [43]:

$$J_{TAT} = A \exp\left(\frac{-8\pi\sqrt{2qm^*}\varnothing_T^3}{3hE}\right) \tag{5}$$

where  $\varnothing_T$  is the trapped energy of electron traps with respect to the conduction band edge,  $A$  is a constant, and  $h$  is Planck’s constant. Shallow traps were reduced through the creation of deep traps via PGA modulation, causing the conduction mechanism to shift toward TAT from PFE after gate annealing treatment as indicated in the band diagram of TAT in Figure 8d [44].

Consequently, the leakage mechanism in the high forward bias region was dominated by FNT across the Al<sub>2</sub>O<sub>3</sub>/SiO<sub>2</sub> gate dielectric layer, as shown in Figure 10b. FNT current density (J<sub>FNT</sub>) can be related to the electric field across the dielectric (E<sub>Di</sub>) by [45]:

$$\ln\left(\frac{J_{FNT}}{E_{Di}^2}\right) = \ln(A') - \frac{B'}{|E_{Di}|} \tag{6}$$

where  $A'$  is a constant,  $B' = 8\pi(2m_n^*(q\varnothing_{eff})^3)^{1/2}/(3qh)$ ,  $m_n^*$  is the effective mass of the electron in the gate dielectric,  $\varnothing_{eff}$  is the effective barrier height of the electrons for

FNT, and  $h$  is Planck's constant. The linear relationship of the  $\ln\left(\frac{I}{V^2}\right)$  vs.  $1/V$  graph in Figure 10b verified the FNT conduction mechanism in Region (V) for the MOS–HEMT after gate annealing modulation. The band edge diagram of FNT is shown in Figure 8e.

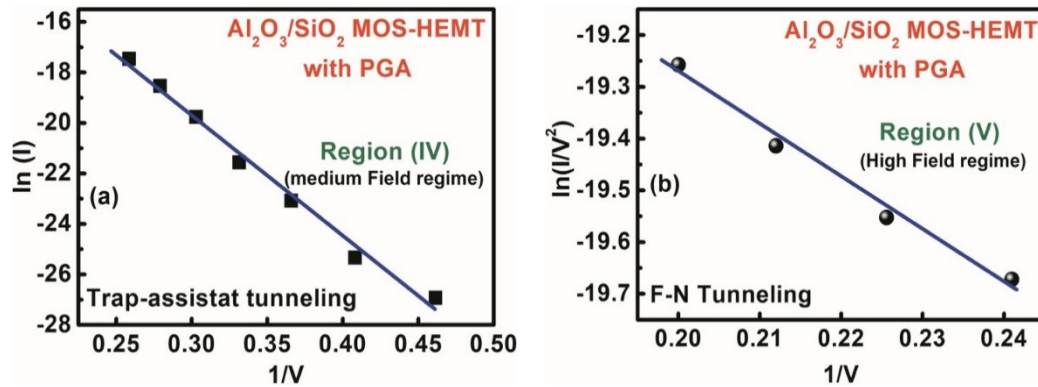


**Figure 10.** Gate leakage conduction mechanism of the Al<sub>2</sub>O<sub>3</sub>/SiO<sub>2</sub> MOS–HEMT after gate annealing treatment (a) region IV, (b) region V.

### 3.3. Gate Leakage Mechanisms in the AlGaIn/GaN HEMT

We also investigated the conduction mechanism of leakage current in the conventional HEMT without PGA by dividing the  $I_G$ – $V_G$  characteristics into different regions, as shown in Figure 7. From Figure 7,  $I_G$  (@  $V_G \leq -4$  V) was clearly saturated due to the saturation of the vertical electrical fields as mentioned previously. The conduction mechanism in Region (II) was confirmed as PFE conduction from the  $\ln(I/V)$  vs.  $V^{1/2}$  graph by following Equation (2), similar to the stack layer MOS–HEMT before PGA treatment, as shown in Figure 11a. In addition, Schottky emission (SE) dominated Region (III) with increasing electric fields at  $V_G > 0$  from the linear slope of  $\ln(I/T^2)$  vs.  $V^{1/2}$ , as shown in Figure 11b, in accordance with the following relation [7]:

$$I_G = A * T^2 \exp\left(\frac{-\varnothing_B}{kT}\right) \exp\left(\frac{S_{SE} \sqrt{V}}{kT \sqrt{d}}\right) \quad (7)$$

$$S_{SE} = \frac{1}{2} \left( \frac{q^3}{\pi \epsilon_0 \epsilon_r} \right)^{1/2} \quad (8)$$

where  $S_{SE}$  is the SE lowering coefficients, and  $\varnothing_B$  is the Schottky barrier height as depicted in the conduction band edge of Region (III) in Figure 8f. In general, SE leads to conduction through the contact interface rather than from bulk material. By contrast, PFE is closely related to the tunneling of carriers and associated with the wide distribution of traps in the band gap of dielectric materials, which originates from impurities and/or structural defects.

To understand the interface quality of the devices, the hysteresis characteristics of the Al<sub>2</sub>O<sub>3</sub>/SiO<sub>2</sub> stack layer MOS–HEMT and the conventional MOS–HEMT were measured (@  $V_G = 6$  V) before and after gate annealing treatment, as shown in Figure 12. Hysteresis behavior was significantly improved after gate annealing modulation in both devices. After gate annealing modulation, the MOS–HEMT exhibited nearly low hysteresis of 0.1 V due to the affective neutralization of the surface caused by the combined effects of TMAH/HCl surface treatment with gate annealing modulation [7]. In addition, a counterclockwise hysteresis was observed in both devices. No surface states were available to capture electrons at a high gate voltage due to the presence of acceptor-like surface states, and electron density in the 2DEG channel was increased to raise the channel current, resulting in counterclockwise hysteresis [7,46].

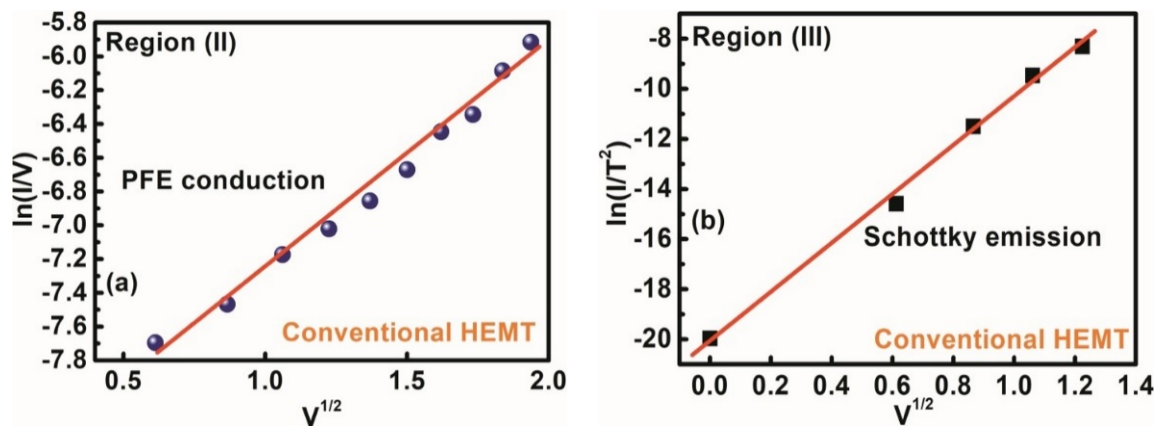


Figure 11. Gate leakage conduction mechanism of the conventional HEMT (a) region II, (b) region III.

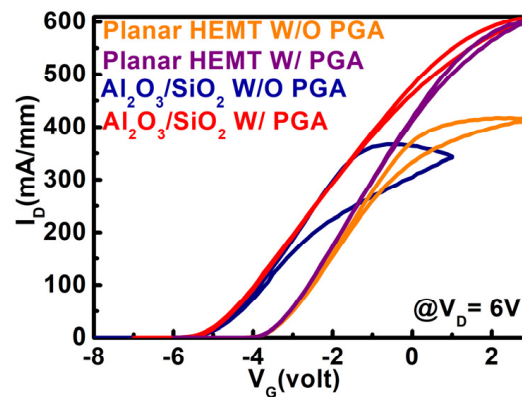
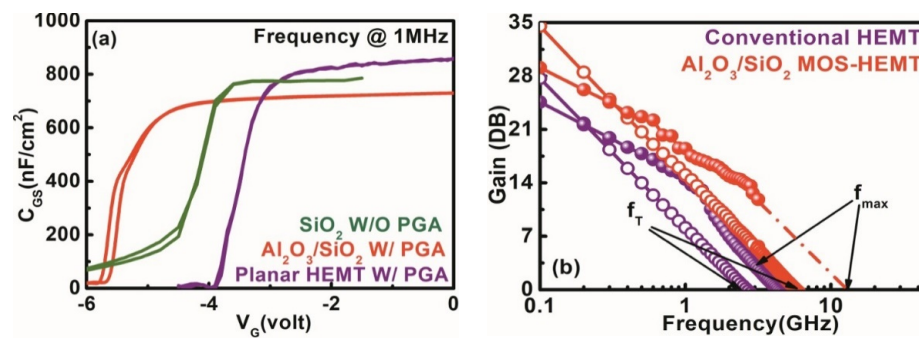


Figure 12. Hysteresis characteristics of the conventional HEMT and  $\text{Al}_2\text{O}_3/\text{SiO}_2$  MOS-HEMT with and without PGA treatment.

To understand the reduction of trap states after dual surface treatment and PGA modulation with the stack layer gate dielectric in the MOS-HEMT compared with that in the conventional HEMT, capacitance-voltage ( $C-V$ ) measurements were performed at 1 MHz for both devices as shown in Figure 13a. The high-frequency performance of the stack layer MOS-HEMT and the conventional HEMT without PGA, and short-circuit current gain ( $|H_{21}|$ ), maximum stable gain/maximum available gain (MSG/MAG) were measured as shown in Figure 13b. The measured cut-off frequency ( $f_t$ ) and maximum oscillation frequency ( $f_{max}$ ) of the MOS-HEMT were 7.5 GHz and 13.5 GHz, while those for the conventional HEMT were only 2.7 GHz and 5 GHz, respectively. The comparatively higher ( $f_{max} \times L_G$ ) was recorded in the MOS-HEMT after PGA modification in contrast with previous reports as indicated in Table 1. The interface state density ( $D_{it}$ ) for the dual surface-treated MOS-HEMT can be extracted from a previously reported formula [47] to be  $1.61 \times 10^{12} \text{ eV}^{-1} \text{ cm}^{-2}$ , which is significantly improved from that of the conventional HEMT ( $1.1 \times 10^{13} \text{ eV}^{-1} \text{ cm}^{-2}$ ). For the  $\text{SiO}_2$  MOS-HEMT,  $D_{it}$  was  $3.8 \times 10^{12} \text{ eV}^{-1} \text{ cm}^{-2}$ . Given the combined effects of dual surface treatment and the stack dielectric layer with gate annealing modulation,  $D_{it}$  was significantly reduced up to one order of magnitude lower in the MOS-HEMT compared with that in the conventional HEMT. Table 1 presents the DC performance and high-frequency comparison of the different gate structure MOS-HEMTs, including the PGA modulated dual surface-treated  $\text{Al}_2\text{O}_3/\text{SiO}_2$  stack layer MOS-HEMT [17,19,31,48–51].



**Figure 13.** (a) Capacitance voltage characteristics of the conventional HEMT and the Al<sub>2</sub>O<sub>3</sub>/SiO<sub>2</sub> MOS-HEMT with gate annealing treatment and SiO<sub>2</sub> MOS-HEMT without PGA treatment. (b) High-frequency characteristics of stack layer MOS-HEMT and conventional HEMT.

**Table 1.** Comparison of DC/RF performances for different gate structure AlGaIn/GaN MOS-HEMTs with dual surface treated Al<sub>2</sub>O<sub>3</sub>/SiO<sub>2</sub> stack layer MOS-HEMT.

Reference	L <sub>G</sub> (μm)	Gate Dielectric (Thickness)	I <sub>D</sub> MAX (mA/mm)	G <sub>M</sub> MAX (mS/mm)	SS (mV/dec)	I <sub>ON</sub> /I <sub>OFF</sub>	Gate Leakage (A/mm)	f <sub>MAX</sub> (GHz)	f <sub>MAX</sub> × L <sub>G</sub> (GHz·μm)
[19]	0.09 (T-gate)	Mg <sub>0.25</sub> Ca <sub>0.75</sub> O (4 nm)	1250	345 (@ V <sub>D</sub> = 9 V)	104	~10 <sup>8</sup>	~10 <sup>-7</sup> (@ V <sub>G</sub> = -7 V)	160	14.4
[27]	1 (rectangular gate)	Al <sub>2</sub> O <sub>3</sub> (12 nm)	853.3	159 (@ V <sub>D</sub> = 7 V)	90.3	~10 <sup>7</sup>	~10 <sup>-8</sup> (@ V <sub>G</sub> = -100 V)	23.4	23.4
[48]	1 (rectangular gate)	HfO <sub>2</sub> /Y <sub>2</sub> O <sub>3</sub> (12/1 nm)	600	4.5 (@ V <sub>D</sub> = 0.05 V)	70	10 <sup>9</sup>	~10 <sup>-10</sup> (@ V <sub>G</sub> = -9 V)	-	-
[31]	0.15 (T-gate)	Al <sub>2</sub> O <sub>3</sub> (7 nm)	859	484 (@ V <sub>D</sub> = 5 V)	-	-	~10 <sup>-8</sup> (@ V <sub>G</sub> = -4 V)	100	15
[49]	1 (rectangular gate)	Al <sub>2</sub> O <sub>3</sub> (20 nm)	855	140.6 (@ V <sub>D</sub> = 7 V)	-	-	~10 <sup>-9</sup> (@ V <sub>G</sub> = -50 V)	19.1	19.1
[50]	0.4 (T-gate)	TiO <sub>2</sub> /NiO (>35 nm)	709	149 (@ V <sub>D</sub> = 10 V)	-	-	~10 <sup>-9</sup> (@ V <sub>G</sub> = -10 V)	40	16
[51]	1 (rectangular gate)	ZrO <sub>2</sub> /Al <sub>2</sub> O <sub>3</sub> (12/1 nm)	847	181 (@ V <sub>D</sub> = 4 V)	95	~10 <sup>7</sup>	-	9.1	9.1
This work	2 (rectangular gate)	Al <sub>2</sub> O <sub>3</sub> /SiO <sub>2</sub> (10/5 nm)	720	120 (@ V <sub>D</sub> = 4 V)	82	10 <sup>9</sup>	10 <sup>-12</sup> (@ V <sub>G</sub> = -12 V)	13.58	27.16

#### 4. Conclusions

In summary, we successfully demonstrated the performance of an Al<sub>2</sub>O<sub>3</sub>/SiO<sub>2</sub> stack layer MOS-HEMT that used TMAH and HCl dual surface treatment prior to gate oxide deposition with PGA modulation. The off-state gate leakage current was remarkably reduced to  $1.5 \times 10^{-12}$  A/mm, which was seven orders of magnitude lower ( $\sim 10^{-5}$  A/mm) than that of the conventional HEMT. A significant reduction in I<sub>G</sub> was observed in MOS-HEMT due to the combined effects of dual surface treatment and the stack gate dielectric layer with gate annealing modulation at 400 °C. In addition, a systematic investigation of the gate leakage conduction mechanism of the conventional HEMT and the MOS-HEMT before and after PGA modulation was conducted. At reverse bias, the PFE conduction mechanism dominated both devices. At low and medium forward bias, the dominant conduction mechanisms were ohmic and PFE, and at higher forward bias, gate leakage was governed by the hopping conduction mechanism for the MOS-HEMT before PGA. By contrast, after the gate annealing treatment of MOS-HEMT, the dominant leakage

conduction mechanism was TAT at the low to medium forward bias region and FNT at the higher forward bias region due to the reduction of shallow traps.

**Author Contributions:** S.M. was responsible for the device preparation, characterization, modeling discussion and writing the draft. P.P. was responsible for the characterization and modeling discussion; K.-W.L. was responsible for the data analysis and editing of the manuscript; Y.-H.W. was the advisor who supervised the progress and paper editing. All authors have read and agreed to the published version of the manuscript.

**Funding:** This research was funded by the Ministry of Science and Technology, Taiwan, grant numbers MOST 106-2221-E-006-219-MY3 and MOST 109-2221-E-06-075-MY2; Transcom Inc., Taiwan, grant number 109S0172; and Materials Analysis Technology Inc. under Contract No. 2021-T-01.

**Institutional Review Board Statement:** Not applicable.

**Informed Consent Statement:** Not applicable.

**Data Availability Statement:** The data presented in this study are available on request from the corresponding author.

**Acknowledgments:** The authors acknowledge the use of the TEM, EDS, and ALD systems belonging to the core facility center of National Cheng-Kung University, Tainan, Taiwan. Taiwan Semiconductor Research Institute of National Applied Research Laboratories, Taiwan for the support of high-frequency measurements and device characterization are also highly appreciated.

**Conflicts of Interest:** The authors declare no conflict of interest.

## References

- Borga, M.; Meneghini, M.; Benazzi, D.; Canato, E.; Püsche, R.; Derluyn, J.; Abid, I.; Medjdoub, F.; Meneghesso, G.; Zanoni, E. Buffer breakdown in GaN-on-Si HEMTs: A comprehensive study based on a sequential growth experiment. *Microelectron. Reliab.* **2019**, *100–101*, 113461. [\[CrossRef\]](#)
- Ardaravicius, L.; Matulionis, A.; Liberis, J.; Kiprijanovic, O.; Ramonas, M.; Eastman, L.F.; Shealy, J.R.; Vertiatichikh, A. Electron drift velocity in AlGaIn/GaN channel at high electric fields. *Appl. Phys. Lett.* **2003**, *83*, 4038–4040. [\[CrossRef\]](#)
- Mazumder, S.; Wang, Y.H. Investigation of HfSiO<sub>x</sub> passivation effect on AlGaIn/GaN HEMT. In Proceedings of the 2020 International Symposium on Devices, Circuits and Systems, ISDCS, Howrah, India, 4–6 March 2020; pp. 1–4.
- Hori, Y.; Yatabe, Z.; Hashizume, T. Characterization of interface states in Al<sub>2</sub>O<sub>3</sub>/AlGaIn/GaN structures for improved performance of high-electron-mobility transistors. *J. Appl. Phys.* **2013**, *114*, 244503. [\[CrossRef\]](#)
- Dutta, G.; DasGupta, N.; DasGupta, A. Gate Leakage Mechanisms in AlInN/GaN and AlGaIn/GaN MIS-HEMTs and Its Modelling. *IEEE Trans. Electron Devices* **2017**, *64*, 3609–3615. [\[CrossRef\]](#)
- Jun, L.; Lei, Z.S.; Han, M.M.; Bin, H.; Lei, Y.X.; Cheng, Z.J.; Hua, M.X.; Yue, H. Trap states induced by reactive ion etching in AlGaIn/GaN high-electron-mobility transistors. *Chin. Phys. B* **2015**, *24*, 117305.
- Reddy, M.S.P.; Park, W.S.; Im, K.S.; Lee, J.H. Dual-surface modification of AlGaIn/GaN HEMTs using TMAH and piranha solutions for enhancing current and 1/f-Noise Characteristics. *IEEE J. Electron Devices Soc.* **2018**, *6*, 791–796. [\[CrossRef\]](#)
- Eller, B.S.; Yang, J.; Nemanich, R.J. Electronic surface and dielectric interface states on GaN and AlGaIn. *J. Vac. Sci. Technol. A* **2013**, *31*, 050807. [\[CrossRef\]](#)
- Koyama, Y.; Hashizume, T.; Hasegawa, H. Formation processes and properties of Schottky and ohmic contacts on *n*-type GaN for field effect transistor applications. *Solid State Electron.* **1999**, *43*, 1483–1488. [\[CrossRef\]](#)
- Rickert, K.A.; Ellis, A.B.; Himpel, F.J.; Sun, J.; Kuech, T.F. n-GaN surface treatments for metal contacts studied via X-ray photoemission spectroscopy. *Appl. Phys. Lett.* **2002**, *80*, 204–206. [\[CrossRef\]](#)
- Hashizume, T.; Ootomo, S.; Oyama, S.; Konishi, M.; Hasegawa, H. Chemistry and electrical properties of surfaces of GaN and GaN/AlGaIn heterostructures. *J. Vac. Sci. Technol. B* **2001**, *19*, 1675–1681. [\[CrossRef\]](#)
- Nepal, N.; Garces, N.Y.; Meyer, D.J.; Hite, J.K.; Mastro, M.A.; Eddy, C.R., Jr. Assessment of GaN surface pre-treatment for atomic layer deposited high-k dielectrics. *Appl. Phys. Exp.* **2011**, *4*, 055802. [\[CrossRef\]](#)
- Ganguly, S.; Verma, J.; Hu, Z.; Xing, H.; Jena, D. Performance enhancement of InAlN/GaN HEMTs by KOH surface treatment. *Appl. Phys. Exp.* **2014**, *7*, 034102. [\[CrossRef\]](#)
- Zhuang, D.; Edgar, J.H. Wet etching of GaN, AlN, and SiC: A review. *Mater. Sci. Eng. R Rep.* **2005**, *48*, 1–46. [\[CrossRef\]](#)
- Son, D.H.; Jo, Y.W.; Won, C.H.; Lee, J.H.; Seo, J.H.; Lee, S.H.; Lim, J.W.; Kim, J.H.; Kang, I.M.; Cristoloveanu, S.; et al. Normally-off AlGaIn/GaN-based MOS-HEMT with self-terminating TMAH wet recess etching. *Solid State Electron.* **2018**, *141*, 7–12. [\[CrossRef\]](#)
- Lee, K.W.; Chou, D.W.; Wu, H.R.; Huang, J.J.; Wang, Y.H.; Houng, M.P.; Chang, S.J.; Su, Y.K. GaN MOSFET with liquid phase deposited oxide gate. *Electron. Lett.* **2002**, *38*, 829–830. [\[CrossRef\]](#)

17. Tsurumi, N.; Ueno, H.; Murata, T.; Ishida, H.; Uemoto, Y.; Ueda, T.; Inoue, K.; Tanaka, T. AlN passivation over AlGaIn/GaN HFETs for surface heat spreading. *IEEE Trans. Electron Devices* **2010**, *57*, 980–985. [[CrossRef](#)]
18. Mazumder, S.; Li, S.H.; Wu, Z.G.; Wang, Y.H. Combined Implications of UV/O<sub>3</sub> Interface Modulation with HfSiO<sub>x</sub> Surface Passivation on AlGaIn/AlN/GaN MOS-HEMT. *Crystals* **2021**, *11*, 136. [[CrossRef](#)]
19. Zhou, H.; Lou, X.; Sutherlin, K.; Summers, J.; Kim, S.B.; Chabak, K.D.; Gordon, R.G.; Ye, P.D. DC and RF Performance of AlGaIn/GaN/SiC MOSHEMTs With Deep Sub-Micron T-Gates and Atomic Layer Epitaxy MgCaO as Gate Dielectric. *IEEE Electron Device Lett.* **2017**, *38*, 1409–1412. [[CrossRef](#)]
20. Yue, Y.; Hao, Y. AlGaIn/GaN MOS-HEMT with HfO<sub>2</sub> Dielectric and Al<sub>2</sub>O<sub>3</sub> Interfacial Passivation Layer Grown by Atomic Layer Deposition. *IEEE Electron Device Lett.* **2008**, *29*, 838–840. [[CrossRef](#)]
21. Dutta, G.; DasGupta, N.; DasGupta, A. Effect of Sputtered-Al<sub>2</sub>O<sub>3</sub> Layer Thickness on the Threshold Voltage of III-Nitride MIS-HEMTs. *IEEE Trans. Electron Devices* **2016**, *63*, 1450–1458. [[CrossRef](#)]
22. Yang, S.K.; Mazumder, S.; Wu, Z.G.; Wang, Y.H. Performance enhancement in N<sub>2</sub> plasma modified AlGaIn/AlN/GaN MOS-HEMT using HfAlO<sub>x</sub> gate dielectric with Γ-shaped gate engineering. *Materials* **2021**, *14*, 1534. [[CrossRef](#)] [[PubMed](#)]
23. Byun, Y.C.; Lee, J.G.; Meng, X.; Lee, J.S.; Lucero, A.T.; Kim, S.J.; Young, C.D.; Kim, M.J.; Kim, J. Low temperature (100 °C) atomic layer deposited-ZrO<sub>2</sub> for recessed gate GaN HEMTs on Si. *Appl. Phys. Lett.* **2017**, *111*, 082905. [[CrossRef](#)]
24. Wu, T.Y.; Lin, S.K.; Sze, P.W.; Huang, J.J.; Chien, W.C.; Hu, C.C.; Tsai, M.J.; Wang, Y.H. AlGaIn/GaN MOSHEMTs with liquid-phase deposited TiO<sub>2</sub> as gate dielectric. *IEEE Trans. Electron Devices* **2009**, *56*, 2911–2916. [[CrossRef](#)]
25. Hashizume, T.; Ootomo, S.; Hasegawa, H. Suppression of current collapse in insulated gate AlGaIn/GaN heterostructure field-effect transistors using ultrathin Al<sub>2</sub>O<sub>3</sub> dielectric. *Appl. Phys. Lett.* **2003**, *83*, 2952–2954. [[CrossRef](#)]
26. Rawat, A.; Meer, M.; Surana, V.K.; Bhardwaj, N.; Pendem, V.; Garigapati, N.S.; Yadav, Y.; Ganguly, S.; Saha, D. Thermally Grown TiO<sub>2</sub> and Al<sub>2</sub>O<sub>3</sub> for GaN-Based MOS-HEMTs. *IEEE Trans. Electron Devices* **2018**, *65*, 3725–3731. [[CrossRef](#)]
27. Liu, H.Y.; Ou, W.C.; Hsu, W.C. Investigation of post oxidation annealing effect on H<sub>2</sub>O<sub>2</sub>-Grown Al<sub>2</sub>O<sub>3</sub>/AlGaIn/GaN MOS-HEMTs. *IEEE J. Electron Devices Soc.* **2016**, *4*, 358–364. [[CrossRef](#)]
28. Liu, Z.H.; Ng, G.I.; Arulkumaran, S.; Maung, Y.K.T.; Zhou, H. Temperature-dependent forward gate current transport in atomic layer-deposited Al<sub>2</sub>O<sub>3</sub>/AlGaIn/GaN metal-insulator-semiconductor high electron mobility transistor. *Appl. Phys. Lett.* **2011**, *98*, 163501-1–163501-3. [[CrossRef](#)]
29. Hua, M.; Liu, C.; Yang, S.; Liu, S.; Fu, K.; Dong, Z.; Cai, Y.; Zhang, B.; Chen, K.J. Characterization of leakage and reliability of SiN<sub>x</sub> gate dielectric by low-pressure chemical vapor deposition for GaN based MIS-HEMTs. *IEEE Trans. Electron Devices* **2015**, *62*, 3215–3222. [[CrossRef](#)]
30. Mazumder, S.; Pal, P.; Tsai, T.J.; Lin, P.C.; Wang, Y.H. A low program voltage enabled flash like AlGaIn/GaN stack layered MIS-HEMTs using trap assisted technique. *ECS J. Solid State Sci. Technol.* **2021**, *10*, 055019. [[CrossRef](#)]
31. Wang, C.; Chen, Y.C.; Hsu, H.T.; Tsao, Y.F.; Lin, Y.C.; Dee, C.F.; Chang, E.Y. Adoption of the Wet Surface Treatment Technique for the Improvement of Device Performance of Enhancement-Mode AlGaIn/GaN MOS-HEMTs for Millimeter-Wave Applications. *Materials* **2021**, *14*, 6558. [[CrossRef](#)]
32. Do, J.W.; Jung, H.W.; Shin, M.J.; Ahn, H.K.; Kim, H.; Kim, R.H.; Cho, K.J.; Chang, S.J.; Min, B.G.; Yoon, H.S.; et al. The effects of tetramethylammonium hydroxide treatment on the performance of recessed-gate AlGaIn/GaN high electron mobility transistors. *Thin Solid Film.* **2017**, *628*, 31–35. [[CrossRef](#)]
33. Sharma, P.; Sundaram, M.M.; Singh, D.; Ahuja, R. Highly Energetic and Stable Gadolinium/Bismuth Molybdate with a Fast Reactive Species, Redox Mechanism of Aqueous Electrolyte. *ACS Appl. Energy Mater.* **2020**, *3*, 12385–12399. [[CrossRef](#)]
34. Manickam, M.; Singh, P.; Issa, T.B.; Thurgate, S.; Marco, R.D. Lithium insertion into manganese dioxide electrode in MnO<sub>2</sub>/Zn aqueous battery: Part I. A preliminary study. *J. Power Source* **2004**, *130*, 254–259. [[CrossRef](#)]
35. Zheng, Y.Y.; Yue, H.; Cheng, Z.J.; Qian, F.; Yu, N.J.; Hua, M.X. A study on Al<sub>2</sub>O<sub>3</sub> passivation in GaN MOS-HEMT by pulsed stress. *Chin. Phys. B* **2008**, *17*, 1405–1409. [[CrossRef](#)]
36. Vetury, R.; Zhang, N.Q.; Keller, S.; Mishra, U.K. The impact of surface states on the DC and RF characteristics of AlGaIn/GaN HFETs. *IEEE Trans. Electron Devices* **2001**, *48*, 560–566. [[CrossRef](#)]
37. Liu, C.; Chor, E.F.; Tan, L.S. Improved DC performance of AlGaIn/GaN high electron mobility transistors using hafnium oxide for surface passivation. *Thin Solid Film.* **2007**, *515*, 4369–4372. [[CrossRef](#)]
38. Ozaki, S.; Makiyama, K.; Ohki, T.; Okamoto, N.; Kumazaki, Y.; Kotani, J.; Kaneki, S.; Nishiguchi, K.; Nakamura, N.; Hara, N.; et al. Improved DC performance and current stability of ultrathin-Al<sub>2</sub>O<sub>3</sub>/InAlN/GaN MOSHEMTs with post-metallization-annealing process. *Semicond. Sci. Technol.* **2020**, *35*, 035027. [[CrossRef](#)]
39. Mazumder, S.; Wu, Z.G.; Pan, P.C.; Li, S.H.; Wang, Y.H. DC performance improvement of nanochannel AlGaIn/AlN/GaN HEMTs with reduced OFF-state leakage current by post-gate annealing modulation. *Semicond. Sci. Technol.* **2021**, *36*, 095003. [[CrossRef](#)]
40. Sze, S.M.; Ng, K.K. *Physics of Semiconductor Devices*, 3rd ed.; Springer Science & Business Media: Berlin, Germany, 2006.
41. Sareni, B.; Krahenbuhl, L.; Beroual, A.; Brosseau, C. Effective dielectric constant of random composite materials. *J. Appl. Phys.* **1997**, *81*, 2375–2383. [[CrossRef](#)]
42. Pal, P.; Mazumder, S.; Huang, C.W.; Lu, D.D.; Wang, Y.H. Impact of Barrier Layer on High Thermal and Mechanical Stability of a Flexible Resistive Memory in Neural Network Application. *ACS Appl. Electron. Mater.* **2021**, *4*, 1072–1081. [[CrossRef](#)]

43. Wang, Q.; Periasamy, K.; Fu, Y.; Chan, Y.T.; Tan, C.M.; Bajalovic, N.; Wang, J.C.; Loke, D.K. Analytical modeling electrical conduction in resistive-switching memory through current-limiting-friendly combination frame works. *AIP Adv.* **2020**, *10*, 085117. [[CrossRef](#)]
44. Kim, H.; Lee, J.; Liu, D.; Lu, W. Gate current leakage and breakdown mechanism in unpassivated AlGa<sub>N</sub>/Ga<sub>N</sub> high electron mobility transistors by post-gate annealing. *Appl. Phys. Lett.* **2005**, *86*, 143505. [[CrossRef](#)]
45. Turuvekere, S.; Karumuri, N.; Rahman, A.A.; Bhattacharya, A.; Dasgupta, A.; DasGupta, N. Gate leakage mechanisms in AlGa<sub>N</sub>/Ga<sub>N</sub> and AlIn<sub>N</sub>/Ga<sub>N</sub> HEMTs: Comparison and modeling. *IEEE Trans. Electron Devices* **2013**, *60*, 3157–3165. [[CrossRef](#)]
46. Chikhaoui, W.; Bluet, J.M.; Bru-Chevallier, C.; Dua, C.; Aubry, R. Deep traps analysis in AlGa<sub>N</sub>/Ga<sub>N</sub> heterostructure transistor. *Phys. Status Solidi C* **2010**, *7*, 92–95. [[CrossRef](#)]
47. Mazumder, S.; Wu, Z.G.; Wang, Y.H. Positive Shifting of V<sub>th</sub> with Enhanced DC Performance in AlGa<sub>N</sub>/Ga<sub>N</sub> Schottky-Gate HEMT through Optimized UV/O<sub>3</sub> Treated Gate Interface and Thermal Engineering. *ECS J. Solid State Electron.* **2022**, *11*, 065002. [[CrossRef](#)]
48. Shi, Y.T.; Xu, W.Z.; Zeng, C.K.; Ren, F.F.; Ye, J.D.; Zhou, D.; Chen, D.J.; Zhang, R.; Zheng, Y.; Lu, H. High-*k* HfO<sub>2</sub>-Based AlGa<sub>N</sub>/Ga<sub>N</sub> MIS-HEMTs With Y<sub>2</sub>O<sub>3</sub> Interfacial Layer for High Gate Controllability and Interface Quality. *IEEE J. Electron Devices Soc.* **2019**, *8*, 15–19. [[CrossRef](#)]
49. Chou, B.Y.; Hsu, W.C.; Liu, H.Y.; Lee, C.S.; Wu, Y.S.; Sun, W.C.; Wei, S.Y.; Yu, S.M.; Chiang, M.H. Investigations of AlGa<sub>N</sub>/Ga<sub>N</sub> MOS-HEMT with Al<sub>2</sub>O<sub>3</sub> deposition by ultrasonic spray pyrolysis method. *Semicond. Sci. Technol.* **2015**, *30*, 015009. [[CrossRef](#)]
50. Meng, D.; Lin, S.; Wen, C.P.; Wang, M.; Wang, J.; Hao, Y.; Zhang, Y.; Lau, K.M.; Wu, W. Low leakage current and high-cut off frequency AlGa<sub>N</sub>/Ga<sub>N</sub> MOSHEMT using submicrometer-footprint thermal oxidized TiO<sub>2</sub>/NiO as gate dielectric. *IEEE Electron Device Lett.* **2013**, *34*, 738–740. [[CrossRef](#)]
51. Huang, C.Y.; Mazumder, S.; Lin, P.C.; Lee, K.W.; Wang, Y.H. Improved electrical characteristics of AlGa<sub>N</sub>/Ga<sub>N</sub> high-electron-mobility transistor with Al<sub>2</sub>O<sub>3</sub>/ZrO<sub>2</sub> stacked gate dielectrics. *Materials* **2022**, *15*, 6895. [[CrossRef](#)]